



## Original Research Paper

Resolved CFD–DEM coupling simulation using Volume Penalisation method<sup>☆</sup>Giang T. Nguyen, Ei L. Chan, Takuya Tsuji, Toshitsugu Tanaka, Kimiaki Washino<sup>\*</sup>

Department of Mechanical Engineering, Osaka University, 2-1 Yamadaoka, Suita, Osaka 565-0871, Japan

## ARTICLE INFO

## Article history:

Received 12 September 2020

Received in revised form 8 November 2020

Accepted 6 December 2020

Available online 25 December 2020

## Keywords:

Resolved CFD–DEM coupling

Volume Penalisation method

Smooth mask function

Optimal permeability

Particulate flow

## ABSTRACT

A resolved CFD–DEM coupling model for the simulation of particulate flows is proposed in this work. The Volume Penalisation (VP) method, which is a family of the continuous forcing Immersed Boundary (IB) method, is employed to express the particle–fluid interaction. A smooth mask function is used to avoid sharp transition between the solid (particle) and fluid domains that may cause numerical oscillation with moving particles. Optimal permeability is employed to reduce the model error associated with the VP method. It is determined as a function of only the interface thickness and fluid kinematic viscosity. The proposed model is accurate, easy to implement with any discretisation scheme, and only requires small computational overhead for particle–fluid interaction. Several simulations are performed to test the validity of the proposed model in various systems, i.e. from dilute to relatively dense flows, and the results show good agreement with the exact solution or empirical correlation. It is found that the error can be scaled with the ratio between the gap and interface thickness. The proposed model is also applied to predict the relative viscosity of suspensions and the density segregation in fluidised beds.

© 2021 The Society of Powder Technology Japan. Published by Elsevier B.V. and The Society of Powder Technology Japan. This is an open access article under the CC BY-NC-ND license (<http://creativecommons.org/licenses/by-nc-nd/4.0/>).

## 1. Introduction

Particle–fluid systems are frequently encountered in many engineering applications such as fluidised beds, pneumatic conveying, cyclone separator, suspensions, particle sedimentation and aerosol dispersion just to name a few. Although the understanding of the particle–fluid interaction plays a vital role in the design and control of such systems, our knowledge today is still limited because of the difficulty in measuring the complex interactions by experiment. Numerical simulation can be a powerful alternative approach to fill the gap.

The computational models for particle–fluid flow could be largely classified into the following two categories: (i) Euler–Euler (E–E) and (ii) Euler–Lagrange (E–L) models. The E–E model, which is also referred to as the Two Fluid Model (TFM) [1,2], treats both particle and fluid phases as inter-penetrating continua and is often employed to investigate the overall flow in large systems. In this model, a constitutive relationship must be predetermined to find particle properties as continuum such as viscosity [3]. Despite

the long history of the research in this field, however, a universal constitutive relationship applicable to different flow regimes is still lacking.

Most of the E–L models couple the Computational Fluid Dynamics (CFD) for fluid and Discrete Element Method (DEM) for particles. DEM is originally proposed by Cundall and Strack [4] and solves Newton's second law of motion for individual particles. There are two types of CFD–DEM model: the unresolved and resolved CFD–DEM models. The former, which is simply known as CFD–DEM, uses locally averaged equations for the fluid phase and an empirical closure is prescribed to express the hydrodynamic forces. This allows to simulate relatively large-scale systems, but the complex flows around the individual particles cannot be captured and the results are only as good as the empirical closure used [5–8]. The latter, which is sometimes called DNS–DEM, resolves the detailed flow around individual particles so that the hydrodynamic forces are directly computed from the resultant flow field rather than an input. Complex phenomena such as particulate flow passing through membrane [9], gas–liquid–solid flow with capillary effect [10–18], heat transfer in dense particulate flow [19] and breakage of aggregated particles [20] are elucidated by the resolved CFD–DEM models. The present research works on the resolved CFD–DEM model.

In order to directly simulate the particle–fluid interaction, the physical boundary between solid (i.e. particles) and fluid is often

<sup>☆</sup> Open Access for this article was sponsored by the Society of Powder Technology, Japan, through the KAKENHI Grant Number 18HP2009/ Grant-in-Aid for Publication of Scientific Research Results, Japan Society for the Promotion of Science, 2021.

<sup>\*</sup> Corresponding author.

E-mail address: [washino.k@mech.eng.osaka-u.ac.jp](mailto:washino.k@mech.eng.osaka-u.ac.jp) (K. Washino).

described by either a body-fitted mesh or the Immersed Boundary (IB) method. The former approach requires a great deal of computational effort on the mesh reconstruction at every time step. This is particularly true if the solid has a complex shape and moves/deforms largely [21]. In addition, since the domain boundaries need to be fitted by the geometrical constraints, the resultant nonorthogonal mesh may contain highly skewed cells which can cause reduction of accuracy or, in the worst-case scenario, numerical instability [22].

In contrast to the body-fitted mesh approach, the IB method, which was early introduced by Peskin [23], can be applied in a fixed mesh regardless the shape and movement of the solid. The IB method can get rid of the problem on mesh reconstruction process and is thereby attractive to many researchers. The impact of the solid on the flow is enforced by solving either discrete or continuous equations, namely the discrete forcing and the continuous forcing approaches [24], respectively. The implementation of the discrete forcing approach totally depends on the discretisation method [25–29] and can be lengthy especially when higher-order schemes are employed [30–32]. In contrast, the continuous forcing approach is independent of the discretisation procedure. The induced force by the solid is directly added into the (continuous) governing equation [33–35] and the equation can be discretised by any major CFD schemes for the finite volume, finite difference, finite element and spectral methods.

The Volume Penalisation (VP) method, which is a family of the continuous forcing IB method, is employed in this study. In the VP method, the fluid and solid domains are distinguished using a mask function  $\chi$ . The originally impermeable solid is then replaced with a permeable medium with low permeability. This introduces the penalty term in the momentum equation for the solid domain [36–39]. In the conventional VP method, a discontinuous mask function is used which is zero or one in the fluid or solid domain, respectively. In this way, the shape of solid boundary can only be discontinuously described in the simulation domain. Furthermore, when moving boundaries are included, numerical oscillation can be induced in the resultant flow field [39–44].

In order to get rid of the aforementioned problem caused by the conventional mask function, a smooth mask function with finite solid–fluid interface is sometimes used [40,45–52]. In this case, the value of the mask function is varied continuously from 0 to 1 across the solid–fluid interface. However, this brings another question: how to determine the permeability? In general, with the discontinuous mask function, the rule of thumb is to use low enough permeability so that only negligible amount of fluid can flow through the solid domain and yet to use high enough permeability so that the simulation can be finished within a reasonable time. Note that the time step interval must be in the same order of or smaller than the value of the permeability to avoid the numerical instability [40]. However, employing excessively low permeability with the smooth mask function makes the penalty term significantly large in the interface. In other words, the interface domain practically becomes solid and the results are dependent on the interface thickness. Most of the studies which use the smooth mask function in literature apply an empirical or trial-and-error approach to determine the permeability [40,45–52]. Only recently, Hester et al. [53] proposed an optimal permeability for a given mask function (and its interface thickness) based on the multiple-scales matched-asymptotics analysis to eliminate the leading order model error, and applied it to the flow past a rotating cylinder in 2D.

The present work is dedicated to develop a resolved CFD–DEM coupling model for the study of particulate flows, which is reasonably accurate, easy to implement with any discretisation scheme and requires small computational overhead for particle–fluid interaction. The VP method with the optimal permeability proposed by

Hester et al. is employed to consider the particle–fluid interaction accurately. The influence of the interface thickness to the accuracy of particulate flow simulation is investigated, which is not thoroughly discussed in literature. The proposed model is validated by performing several test simulations from dilute to dense particulate systems. It is also applied for the prediction of the relative viscosity of suspensions with different packing fraction and the analysis of the density segregation in fluidised beds.

## 2. Numerical simulation model

### 2.1. CFD governing equations

The fluid is assumed to be isothermal and incompressible. The continuity and momentum equations for the fluid phase are given as follows:

- Continuity equation

$$\nabla \cdot \mathbf{U} = 0 \quad (1)$$

- Momentum equation

$$\frac{\partial}{\partial t} (\rho_f \mathbf{U}) + \nabla \cdot (\rho_f \mathbf{U} \mathbf{U}) = -\nabla p + \nabla \cdot \boldsymbol{\tau} + \mathbf{f}_{vp} + \rho_f \mathbf{g} \quad (2)$$

where  $\mathbf{U}$  is the fluid velocity,  $p$  is the pressure,  $\boldsymbol{\tau}$  is the viscous stress tensor,  $t$  is the time,  $\rho_f$  is the fluid density,  $\mathbf{g}$  is the gravitational acceleration and  $\mathbf{f}_{vp}$  is the penalty term. More details about the penalty term can be found in Section 2.3. The fluid is assumed to be Newtonian and the viscous stress tensor is given by the following expression:

$$\boldsymbol{\tau} = \mu (\nabla \mathbf{U} + \nabla \mathbf{U}^T) \quad (3)$$

where  $\mu$  is the fluid dynamic viscosity and the superscript T denotes the transposition of a tensor.

### 2.2. DEM governing equations

DEM is originally proposed by Cundall and Stack [4] and used in this study to model the particles flow. In DEM, the translational and rotational motions of a particle  $i$  are governed by the Newton's second law of motion as follows:

$$m_{pi} \dot{\mathbf{v}}_{pi} = \sum_j \mathbf{F}_{cij} + \mathbf{F}_{fi} + \mathbf{F}_{bi} + \mathbf{F}_{gi} \quad (4)$$

$$I_{pi} \dot{\boldsymbol{\omega}}_{pi} = \sum_j \mathbf{T}_{cij} + \mathbf{T}_{fi} \quad (5)$$

where  $m_p$  is the particle mass,  $I_p$  is the particle moment of inertia,  $\mathbf{v}_p$  and  $\boldsymbol{\omega}_p$  are the translational and angular velocities of the particle, respectively,  $\mathbf{F}_c$  is the contact force,  $\mathbf{F}_f$  is the fluid force,  $\mathbf{F}_b$  is the buoyancy force,  $\mathbf{F}_g$  is the gravitational force,  $\mathbf{T}_c$  is the contact torque and  $\mathbf{T}_f$  is the fluid torque. The non-linear spring-dashpot model is employed for the contact force as proposed by Tsuji et al. [54]: the normal force is modelled by the Hertzian contact theory [55] whilst the Mindlin model [56] is used for the tangential force. The fluid force and torque acting on the particle can be determined by integrating the counteracting force of the penalty force and its torque, respectively, over the particle volume as follows:

$$\mathbf{F}_{fi} = - \int_{V_{pi}} \mathbf{f}_{vp} dV \quad (6)$$

$$\mathbf{T}_{fi} = - \int_{V_{pi}} \mathbf{r} \times \mathbf{f}_{vp} dV \quad (7)$$

where  $V_p$  is the volume of the particle and  $\mathbf{r}$  is the relative position from the centre of gravity of the particle.

### 2.3. Penalty term and optimal permeability

The VP method approximates the no-slip boundary condition by considering the penalty term in the solid domain. The penalty term  $\mathbf{f}_{vp}$  in Eq. (2) is often calculated by the mask function, the fluid density, the relative velocity between the solid and fluid and the permeability as [36]:

$$\mathbf{f}_{vp} = \frac{\chi \rho_f}{\eta} (\mathbf{U}_{solid} - \mathbf{U}) \quad (8)$$

where  $\eta$  is the permeability which governs the fluid penetration into the solid domain,  $\chi$  is the mask function and  $\mathbf{U}_{solid}$  is the solid velocity calculated from the particle velocity as:

$$\mathbf{U}_{solid} = \mathbf{v}_p + \mathbf{r} \times \boldsymbol{\omega}_p \quad (9)$$

The physical interpretation of the penalty term in Eq. (8) proposed in [36] corresponds to the Darcy law of the fluid flow in the solid domain considered as a porous media. The small permeability imposes on the fluid velocity to approach the solid velocity. The penalty term is activated in solid domain or vanished in the fluid domain by the mask function.

As seen in Fig. 1(a), the discontinuous mask function  $\chi$  applied in the conventional VP method sharply divides the simulation domain into the fluid domain  $\Omega_f$  and the solid domain  $\Omega_s$  in which  $\chi = 0$  and 1, respectively. On the other hand, the value of the smooth mask function varies rapidly yet continuously from 0 to 1 over the finite interface region  $\Delta\Omega$  as illustrated in Fig. 1(b). The hyperbolic tangent function is used for the mask function in this study:

$$\chi = \frac{1}{2} \left\{ 1 - \tanh \left( \frac{\sigma}{\delta} \right) \right\} \quad (10)$$

where  $\sigma$  is the signed distance (positive in the fluid domain and negative in the solid domain) from the real particle surface and  $\delta$  is the thickness parameter. The resultant mask function is shown in Fig. 2. The interface thickness is proportional to the thickness parameter.

The permeability  $\eta$  is determined based on the work by Hester et al [53], which can eliminate the leading order model error based on the multiple-scales matched-asymptotics analysis. This is called

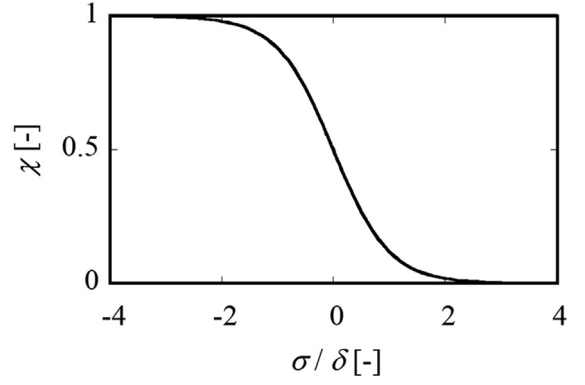


Fig. 2. Smooth mask function as a function of the signed distance from the particle surface normalised with the thickness parameter.

optimal permeability in this paper. We only highlight the key idea for the derivation of the optimal permeability here and the readers may refer to the literature [53] for more details. First, the following dimensionless parameters are defined:

$$\text{Re} = \frac{U_c L_c}{\nu} \quad (11)$$

$$\zeta = \frac{\eta U_c}{L_c} \quad (12)$$

$$\varepsilon = \frac{\sqrt{\nu \eta}}{L_c} \quad (13)$$

where  $U_c$  and  $L_c$  are the characteristic velocity and length scales and  $\nu$  is the kinematic viscosity of the fluid.  $\text{Re}$  is the Reynolds number,  $\zeta$  is the dimensionless damping time scale and  $\varepsilon$  is the dimensionless damping length scale. The continuity and momentum equations are then rewritten in the dimensionless form as:

$$\nabla^* \cdot \mathbf{U}^* = 0 \quad (14)$$

$$\frac{\partial \mathbf{U}^*}{\partial t^*} + \mathbf{U}^* \cdot \nabla^* \mathbf{U}^* = -\nabla^* p^* + \frac{1}{\text{Re}} \nabla^{*2} \mathbf{U}^* + \frac{\chi}{\zeta} (\mathbf{U}_{solid}^* - \mathbf{U}^*) + \mathbf{g}^* \quad (15)$$

where the superscript  $*$  indicates the dimensionless variables. Now, a signed distance coordinate system is introduced. The dimensionless signed distance is first defined as:

$$\sigma^* = \sigma / L_c \quad (16)$$

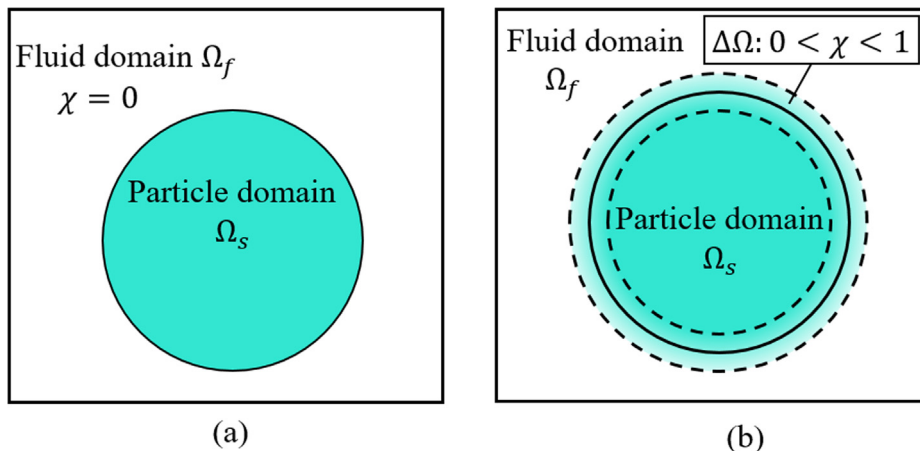


Fig. 1. (a) the discontinuous mask function distinguishing the fluid domain  $\Omega_f$  and solid domain  $\Omega_s$  and (b) the smooth mask function with the interface region  $\Delta\Omega$  (bounded by the dashed lines) while the mask function  $\chi$  becomes 0.5 at the location of the real particle surface as indicated by the solid line.

The solid surface is then parametrised by some orthogonal surface coordinates, say  $s_1$  and  $s_2$ . This signed distance coordinate system allows to define the components in the normal and tangential directions of any quantity and differential operator. For example, the velocity is decomposed as follows:

$$\mathbf{U}^* = \mathbf{U}_\sigma^* + \mathbf{U}_\perp^* \quad (17)$$

where the subscripts  $\sigma$  and  $\perp$  denote the normal and tangential components, respectively. In the interface region, the dimensionless signed distance is rescaled as:

$$\xi = \sigma^*/\varepsilon \quad (18)$$

Using on the asymptotic matching, the leading order normal velocity is zero and the momentum equation takes the following form in terms of the tangential velocity:

$$(\chi - \partial_\xi^2)U_{\perp 0}^*(\xi) = 0 \quad (19)$$

where the subscript 0 denotes the leading order,  $\mathbf{U}_{\perp 0}^* = U_{\perp 0}^*(\xi)\mathbf{t}_\perp$ ,  $\mathbf{t}_\perp$  is the tangential direction vector and the operator  $\partial_\xi$  is the partial derivative in the rescaled normal direction. The physically acceptable solutions of Eq. (19) in the limiting cases are given as:

$$U_{\perp 0}^*(\xi \rightarrow -\infty) = be^{\xi} \quad (20)$$

$$U_{\perp 0}^*(\xi \rightarrow +\infty) = \alpha(\xi - \ell^*) \quad (21)$$

where  $b$ ,  $\alpha$  and  $\ell^*$  are the integral constants.  $\ell^*$  is called the displacement length and defined as the leading order model error since it does not appear in the true no-slip boundary condition. The following mask function can eliminate the displacement length:

$$\chi = \frac{1}{2} \left\{ 1 - \tanh \left( \frac{2\xi}{2.648228} \right) \right\} \quad (22)$$

From Eqs. (10), (13), (16), (18) and (22), the optimal permeability is obtained in the following form:

$$\eta \approx 0.57 \frac{\delta^2}{\nu} \quad (23)$$

The optimal permeability shown in Eq. (23) is a function of only two parameters: the thickness parameter  $\delta$  and the fluid kinematic viscosity  $\nu$ . When the optimal permeability is applied to the 2D flow between parallel plates, the velocity profile is in good agreement with the theoretical parabola as shown in Fig. 3.

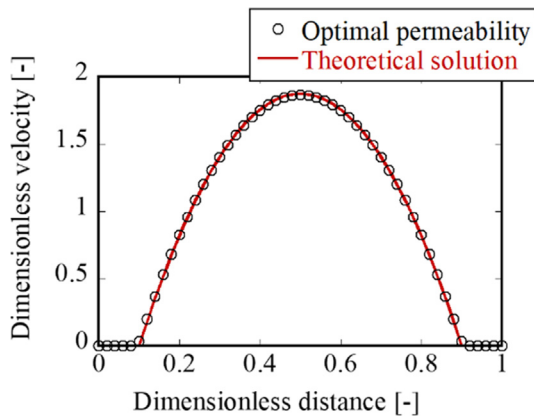


Fig. 3. Velocity profile of the flow between two parallel plates.  $Re = 0.5$  and the thickness parameter is chosen as 80 times smaller than the distance between two plates.

## 2.4. Numerical solution procedure

The proposed model is implemented in open-source CFD and DEM solvers: OpenFOAM for the fluid phase and LIGGGHTS for the particle phase. OpenFOAM uses the finite volume method to discretise the continuity and momentum equations although the VP method is a family of the continuous forcing IB method and any discretisation method is applicable. The PIMPLE algorithm [57], which is the combination of PISO [58] (Pressure Implicit Split Operator) and SIMPLE [59] (Semi-Implicit Method for Pressure Linked Equations) algorithms, is used for the pressure–velocity coupling. The equation of motion for particles is solved by using the velocity-Verlet algorithm. The simulation time step for CFD is kept to be smaller than the optimal permeability calculated by Eq. (23) while the time step for DEM is determined based on the Rayleigh time [60] with a safety factor of 0.1. It only requires simple steps to couple the CFD and DEM solvers. A solution flow chart can be found in Fig. 4 and the solution procedure is summarised below:

- (i) Transfer the particles velocity and position from the DEM solver to the CFD solver.
- (ii) Calculate the solid velocity and mask function fields by Eqs. (9) and (10), respectively.

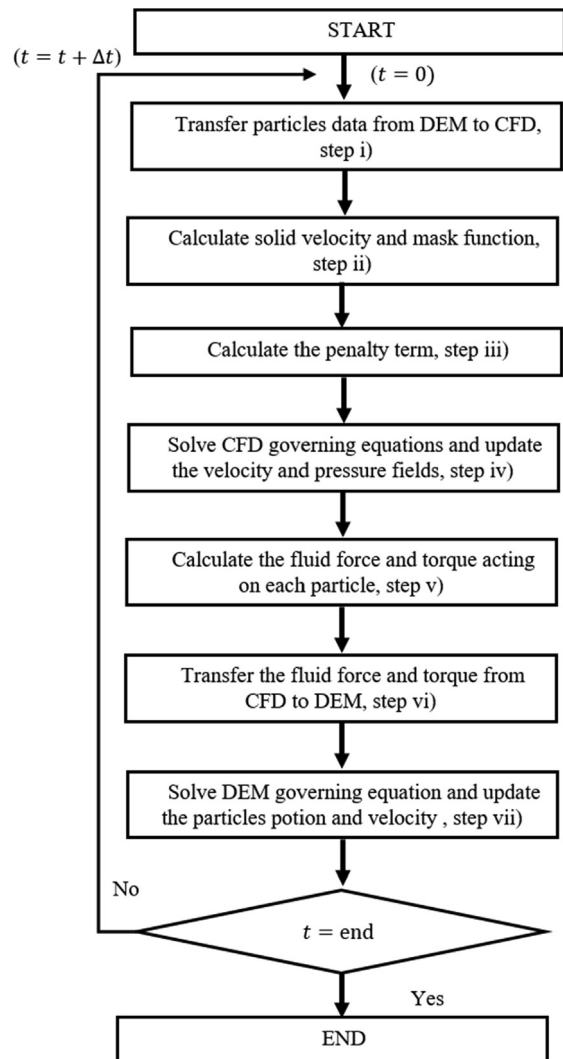


Fig. 4. Numerical solution flow chart of the resolved CFD–DEM model proposed.



- (iii) Calculate the penalty term by Eq. (8).
- (iv) Solve the continuity and momentum equations to update the velocity and pressure fields.
- (v) Calculate the fluid force and torque acting on each particle by Eqs. (6) and (7), respectively
- (vi) Transfer the fluid force and torque from the CFD solver to the DEM solver.
- (vii) Solve the equation of motion for particles to update the position and velocity.
- (viii) Increment the time and return to step i).

### 3. Simulation results

#### 3.1. Flow past a stationary single particle

The present work focuses on the development of the resolved CFD–DEM model with the VP method for particulate systems. The first validation test we present is a stationary single particle with diameter  $d_p$  placed in a uniform flow. As depicted in Fig. 5, the particle–fluid interface is smeared over a finite thickness by controlling the thickness parameter  $\delta$  as  $d_p/20$ ,  $d_p/40$ ,  $d_p/80$  and  $d_p/160$ .

A schematic diagram of the system is shown in Fig. 6(a). A constant velocity is applied at the inlet while zero velocity gradient is applied at all the other boundaries. The pressure is set to zero at the outlet and takes zero gradient for all the other boundaries. The Reynolds number  $Re$  is defined as:

$$Re = \frac{d_p U}{\nu} \quad (24)$$

where  $U$  is the inlet velocity.

It is confirmed in advance that the simulation domain is sufficiently large so that the results are not sensitive to the boundary effects. In order to reduce the calculation cost, local mesh refinement is applied in the simulation domain as shown in Fig. 6(b). The finest mesh domain has edge length of  $8 \times d_p$  and the centre is collocated with that of the particle. From the finest mesh domain, the cell size gradually increases until it reaches that of the unrefined (i.e. background) mesh. The cell size of the unrefined mesh is  $3 \times d_p$ .  $Re$  is varied from 0.001 to 100 and the resultant drag coefficients are compared to the empirical model of Schiller & Naumann [61]. At the steady state, the drag coefficient  $C_D$  is calculated by the following expression:

$$C_D = \frac{2F_D}{\rho U^2 A} \quad (25)$$

where  $F_D$  is the calculated fluid force acting on the particle and  $A$  is the projected area of the particle.

The mesh independency is checked for  $Re = 0.01$  and  $Re = 100$  cases representing the low and high Reynolds numbers tested, respectively. The resolution is defined as the ratio of the particle diameter  $d_p$  to the smallest cell size. As presented in Fig. 7(a) and

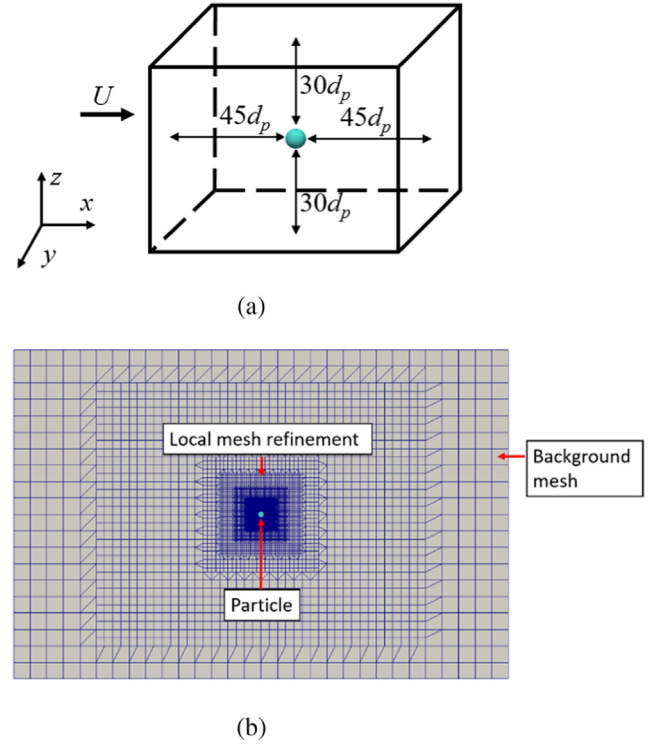


Fig. 6. (a) Schematic diagram of the flow past a stationary single particle and (b) cross section view of the locally refined mesh.

(b), the resultant drag coefficient is converged at around the resolution of 10 to 20 (depending on the thickness parameter) in all the cases. Therefore, the resolution of 20 is applied for the following results in this section to ensure the mesh independency. Note that the drag coefficient  $C_D$  is not sensitive to the thickness parameter when  $Re = 0.01$ . However, when  $Re = 100$ , the larger  $\delta$  gives slightly larger  $C_D$ . In general, the thickness of the boundary layer decreases when Reynolds number is increased. Therefore, employing small interface thickness may be required to resolve the flow in the boundary layer properly.

As shown in Fig. 8, the computed  $C_D$  values obtained from the proposed model agree well with the empirical model of Shiller & Naumann [61] as well as the simulation results reported in literature [11,12]. It is also found that the resultant drag coefficients are not very sensitive to the selection of the thickness parameter. This implies that the optimal permeability given by Eq. (23) is valid in this  $Re$  range. It is worth noting that employing a small thickness parameter is, on the one hand, more advantageous since the particle shape can be sharply described. This is especially important when the inter-particle (or particle–wall) distance is small as discussed in the following sections. On the other hand, the simulation time step can be larger when the thickness parameter is increased

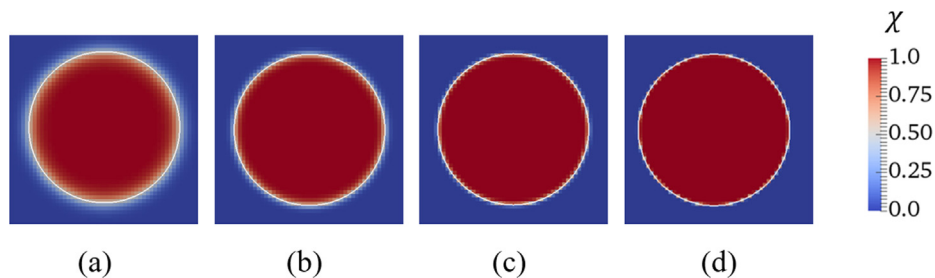
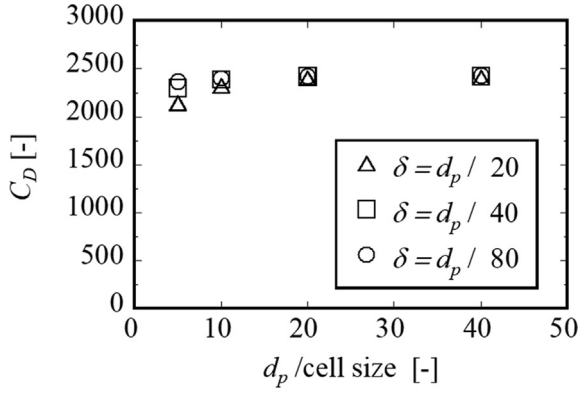
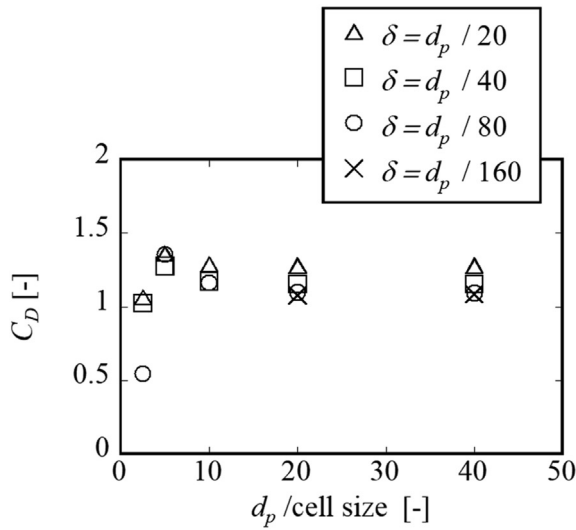


Fig. 5. The mask function with different thickness parameter  $\delta$ ; (a)  $\delta = d_p/20$ , (b)  $\delta = d_p/40$ , (c)  $\delta = d_p/80$  and (d)  $d_p/160$ .



(a)



(b)

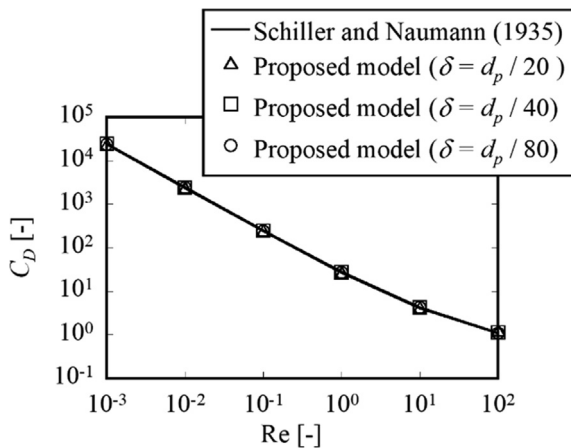
Fig. 7. Mesh independence test; (a)  $Re = 0.01$  and (b)  $Re = 100$ .

Fig. 8. Comparison between the computed drag coefficient obtained from the proposed model and the empirical model of Schiller &amp; Naumann [61].

since the time step is restricted by the permeability [62]. Therefore, it is preferred to use larger thickness parameter if it does not influence the results, which is the case in Fig. 8.

### 3.2. Flow through a periodic array of stationary particles

The simulation results in the preceding section prove that the proposed model can reasonably simulate the flow around a single particle. The proposed model is applied for the flow through a periodic array of particles with the packing fraction  $\phi$  up to 0.68 in this section. Simple Cubic (SC) and Face-Centred Cubic (FCC) arrays of stationary particles are considered in this work. Schematics of SC and FCC arrays are presented in Fig. 9. In the SC array, five particles are aligned in a simulation domain with equal separation distance, and  $\phi$  is varied from 0.2 to 0.5 by changing the particle size. However, the maximum packing fraction of the SC array is approximately 0.52. The FCC array is used for the higher packing fraction: 0.6 and 0.68.

Periodic boundary conditions are applied in the both  $y$ - and  $z$ -directions. A constant velocity is applied at the inlet in the  $x$ -direction whilst zero velocity gradient is set at the outlet. The pressure is set to zero at the outlet and takes zero gradient at the inlet. The Reynolds numbers calculated by Eq. (24) are kept to be less than 0.5 in all cases. The fluid flows through the stationary particles in a zero-gravity field. The fluid force acting on the central particle of the array is nondimensionalized by the following equation [63]:

$$K = \frac{F_D}{3\pi\mu U d_p} \quad (26)$$

A packed column is often modelled as a bundle of tangled tubes [64,65]. The tubes radius is replaced by an effective pore radius  $r_{eff}$ , which is determined as [66]:

$$r_{eff} = \frac{2(1 - \phi)}{\phi \rho_p A_p} \quad (27)$$

where  $\rho_p$  is the density of the particle and  $A_p = 6/(d_p \rho_p)$  is the specific surface area of the particle. In this case, uniform meshes are used and the resolution of the simulation is defined as the ratio of  $r_{eff}$  to the cell size.

Fig. 10 shows the dependency of the dimensionless fluid force on the resolution with different thickness parameters at packing fractions of 0.2 and 0.6 for the SC and FCC arrays, respectively. The results show that  $K$  is converged at the resolution of 10 in all the cases. Therefore, the resolution of 10 is ensured in the following results in this section.

The fluid flow through a small gap between particles becomes important when the packing fraction increases. Hence, the solid-fluid interface thickness may have a significant impact on the resultant fluid force. The influence of the thickness parameter on

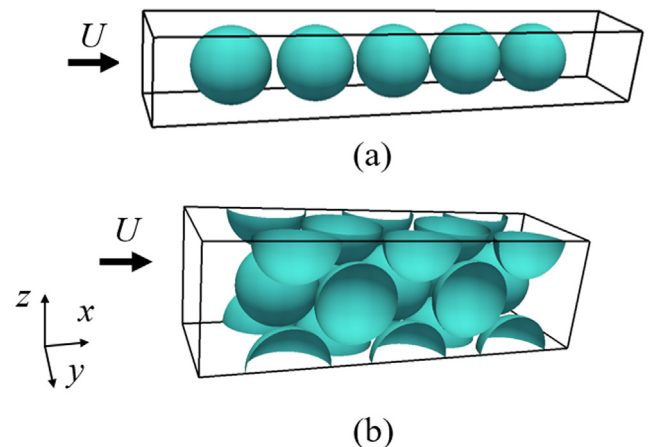


Fig. 9. Schematics of the flow through the (a) SC and (b) FCC arrays.

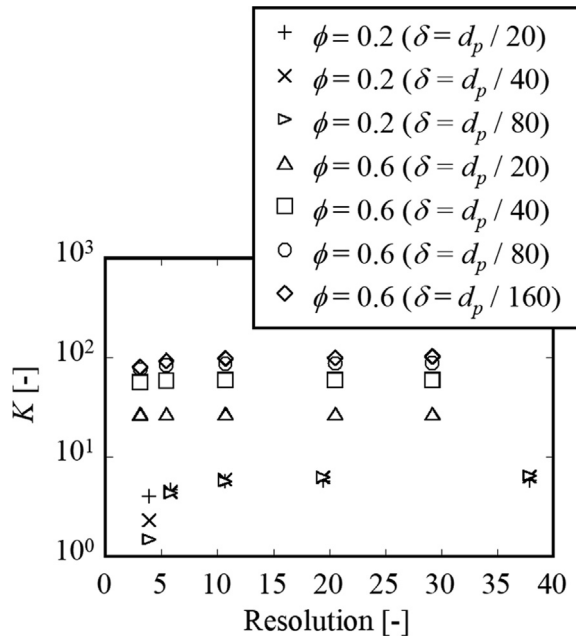


Fig. 10. Relationship between dimensionless fluid force and the resolution.  $\phi = 0.2$  and  $0.6$  for SC and FCC arrays, respectively.

the dimensionless fluid force is shown in Fig. 11 and Fig. 12 for the SC and FCC arrays, respectively. In the SC array, the difference due to the thickness parameter is marginal at the low packing fraction (e.g.  $\phi = 0.2$ ). However, it has an impact on  $K$  when the packing fraction is larger than  $0.3$  and the smaller thickness parameter yields better agreement with the data of Zick and Homay [63], which is obtained from the boundary integral method. The thickness parameter of  $d_p/80$  provides sufficiently small particle–fluid interface region so that the fluid flow can be resolved correctly at the small gap between particles when the packing fraction is up to  $0.4$ , as seen in Fig. 11. However, it even requires smaller thickness parameter ( $d_p/160$ ) in the case of packing fraction from  $0.5$  to  $0.6$  (see Fig. 11 and Fig. 12). When the packing fraction is  $0.68$ ,  $d_p/320$  is needed since the gap between particles become tiny, as seen in Fig. 12. It is proven that the proposed model can simulate

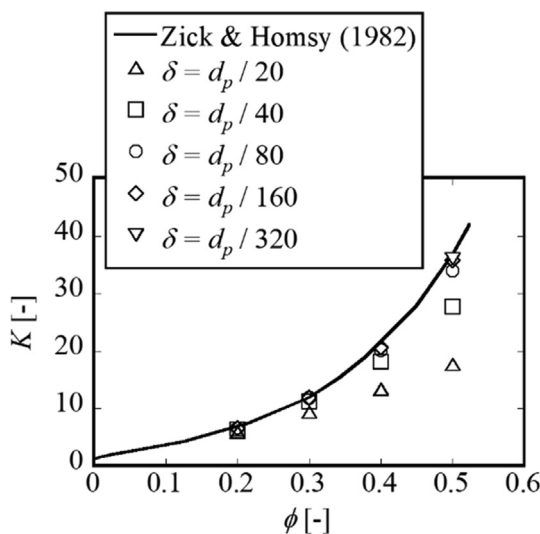


Fig. 11. Comparison of computed dimensionless fluid force and Zick & Homay's study for SC arrays.

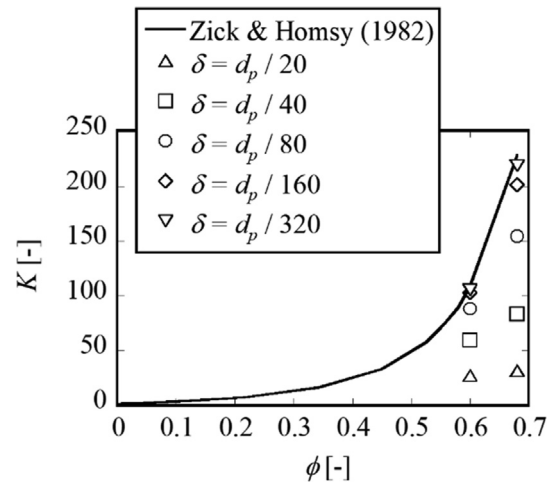


Fig. 12. Comparison of computed dimensionless fluid force and Zick & Homay's study for FCC arrays.

the flow through the packed particles from dilute to dense cases when the proper thickness parameter is appointed. However, it is worth noting that there is no relative movement between particles in the simulations presented in this section. When particles are moving, the lubrication effect should have an impact, which is discussed in the following section.

### 3.3. A particle approaching to a plane wall

In Section 3.1 and 3.2, fixed particles are used to show the validity of the proposed model. In this section, we take one step forward and examine a case with a moving particle: a particle approaching to a plane wall. Simulating this seemingly simple system is actually very challenging due to the well-known lubrication effect caused by the drainage of the interstitial fluid in the small gap between the particle and wall. It has been said that the numerical cells should be smaller than  $0.1\%$  of the particle size to properly capture the lubrication effect, which is practically impossible to run simulation within a reasonable time scale with the current computer power. Therefore, most of the simulations in literature are performed using meshes whose cell size is around  $1 \sim 10\%$  of the particle size. This section mainly focuses on the error related to the lack of resolution with such coarse meshes.

Fig. 13 illustrates a cubic simulation domain whose edge length is  $4.8 \times d_p$ . The VP method is used for the particle whilst the no-slip condition is applied at the bottom wall. Zero velocity gradient is used at all the other boundaries. The pressure is set to zero at the top wall and takes zero gradient for all the other boundaries. The initial position of the particle is one  $d_p$  away from the bottom wall. The particle moves downwards in the negative  $z$ -direction at a constant velocity  $v_p$ . The Reynolds number used is

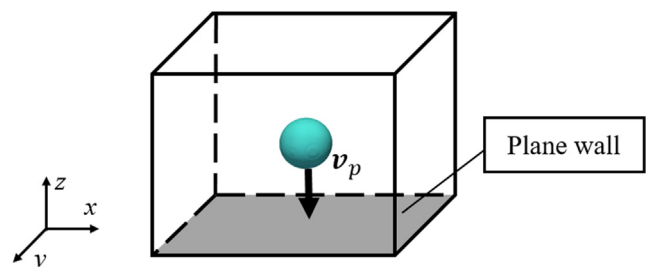


Fig. 13. Schematic diagram of a particle approaching to a plane wall.

$Re = \frac{d_p v_p}{\nu} = 0.1$ . Gravity is not considered in the simulation. The resolution tested (ratio of the particle to the cell size) is 20 and 40, and the thickness parameter is varied as  $d_p/20$ ,  $d_p/40$  and  $d_p/80$ . The fluid force acting on the particle is normalised using the Stokes drag as:

$$F^* = \frac{F_D}{3\pi\mu v_p d_p} \quad (28)$$

The resultant dimensionless fluid force is compared to the exact solution proposed by Brenner [67] written in the dimensionless form as follows:

$$F^* = \frac{4}{3} \sinh \alpha \sum_{n=1}^{\infty} \frac{n(n+1)}{(2n-1)(2n+3)} f(n) \quad (29)$$

$$f(n) = \frac{4 \cosh^2(n + \frac{1}{2})\alpha + (2n+1)^2 \sinh^2 \alpha}{2 \sinh(2n+1)\alpha - (2n+1) \sinh 2\alpha} - 1 \quad (30)$$

where  $\alpha = \cosh^{-1}(h/d_p)$  and  $h$  is the distance from particle centre to the plane wall.

Fig. 14 shows the dimensionless fluid force acting on the particle as a function of the gap normalised with the particle diameter. In all the cases, the simulation results show a good agreement with the exact solution when the gap between the particle and wall is sufficiently large. However,  $F^*$  starts to deviate from the exact solution as the gap gets smaller. The deviation occurs sooner in the case of larger thickness parameter since the interface thickness becomes comparable to the gap. On the other hand, comparing the results between the resolutions of 20 and 40 with the same thickness parameter, the computed fluid forces are almost the same. This means that smaller thickness parameter is required to properly resolve the flow in the small gap although it requires longer simulation time as discussed in Section 3.1.

According to Fig. 14, it can be said that the thickness parameter is the dominant factor to cause the error. Fig. 15 shows the error of the computed fluid force from the exact solution as a function of the gap normalised by the thickness parameter. It can be clearly seen that all the results are unified and fall into one curve. This means that the error can be universally characterised only by the ratio between the gap and thickness parameter regardless the res-

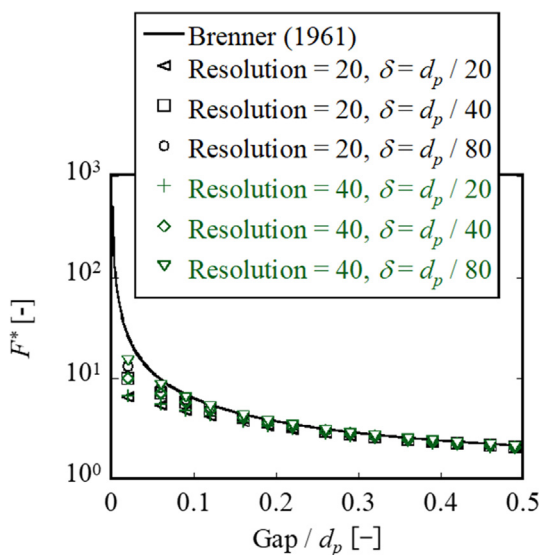


Fig. 14. The dimensionless fluid force acting on the particle with difference thickness parameters and resolutions when the particle approaches to the bottom wall with a constant velocity.

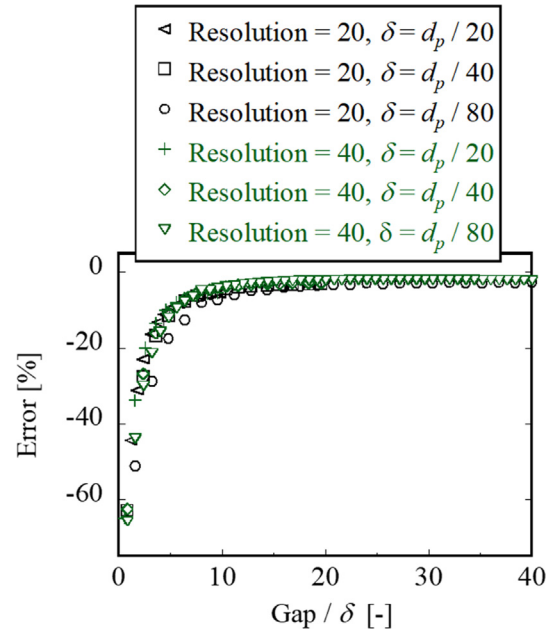


Fig. 15. The error of the computed fluid force acting on the particle when it approaches to very near the plane wall at resolution of 20 and 40.

olution. The error increases rapidly when the particle gets closer to the plane wall: it becomes 5% roughly when the gap to thickness parameter ratio is 10 and becomes 10% roughly when the ratio is 5.

One way to further improve the accuracy of the simulation is to introduce the lubrication force model [43,68–72], i.e. the supplemental force model based on the solution of the lubrication equation. Typically, these lubrication models are resolution-dependent, that is, the gap to cell size ratio is used as a parameter. However, the results in this section reveals that it is important to use the gap to thickness parameter ratio instead if the interface has a thickness. The development and implementation of the lubrication force model is left in the future work and no further discussion is made in this paper.

### 3.4. Relative viscosity of suspensions

The rheology of fluid is characterized by the viscosity which is defined as the ratio between shear stress and shear rate. When particles are suspended in fluid, the viscosity of the suspension is often replaced by the effective viscosity. The relative viscosity,  $\mu_r$ , is defined as the ratio of the effective viscosity to the viscosity of the suspending media. Since suspensions are of paramount importance in many processes [73], the rheological behaviours of suspensions have been intensively studied [74]. The linear dependency of the relative viscosity to packing fraction in very dilute systems is widely known as the Einstein equation [75]. For higher concentration cases, the relative viscosity of suspensions grows non-linearly with packing fraction [73,76–79]. In this section, the proposed model is applied for the prediction of the relative viscosity of suspensions in a simple shear flow.

A schematic of suspension in a simple shear flow is shown in Fig. 16. The no-slip boundaries are applied at the top and bottom walls which move with a constant velocity in the opposite directions to each other. The Reynolds number is  $Re = \frac{2UH}{\nu} = 7$  where  $H$  is the distance between the top and bottom walls. The depth in the  $y$ -direction is 5 mm and the height in the  $z$ -direction is  $H = 7$  mm. The wall velocity is  $U = 0.005$  m/s. Periodic boundary conditions are applied in the  $x$ - and  $y$ -directions. The particles are randomly generated in the entire simulation domain at the



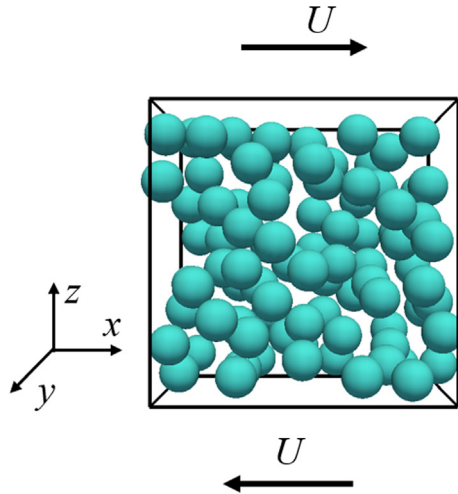


Fig. 16. Schematic of suspension in a simple shear flow.

beginning of each simulation. Gravity, inter-particle cohesion and electrostatic forces as well as the Brownian motion are not considered in the simulation. The fluid and solid properties are presented in Table 1.

The packing fraction  $\phi$  is varied from 0.0125 to 0.42 by changing the number of particles while the resolution (ratio of the effective radius, Eq. (27), to the cell size) is kept more than 20 so that the simulations are mesh-independent based on Fig. 10. The thickness parameter is  $d_p/80$  which is determined based on Fig. 11 with the packing fraction of roughly 0.4. The simulation results are compared to the experiment performed by Yoshida et al. [79] as well as the Einstein equation and the empirical equation of Mori & Ootake [80] defined by Eqs. (31) and (32), respectively.

$$\mu_r = 1 + \frac{5}{2}\phi \quad (31)$$

$$\mu_r = 1 + \frac{3\phi}{1 - \frac{\phi}{0.52}} \quad (32)$$

The results are shown in Fig. 17. When the packing fraction is less than 0.05, the simulation results are well-matched with the Einstein equation. However, the computed  $\mu_r$  starts to deviate from the Einstein equation at higher packing fraction since the hydrodynamic interactions between the particles become more prominent. Good agreement can be seen between the simulation results and the experiment results as well as the Mori & Ootake equation with  $\phi$  up to around  $\phi = 0.3$ . However, the proposed model slightly underestimates the relative viscosity at  $\phi = 0.42$ . The potential reasons are the lubrication effect as well as the effect of the top and bottom walls. It can be concluded that the resolved CFD-DEM model can

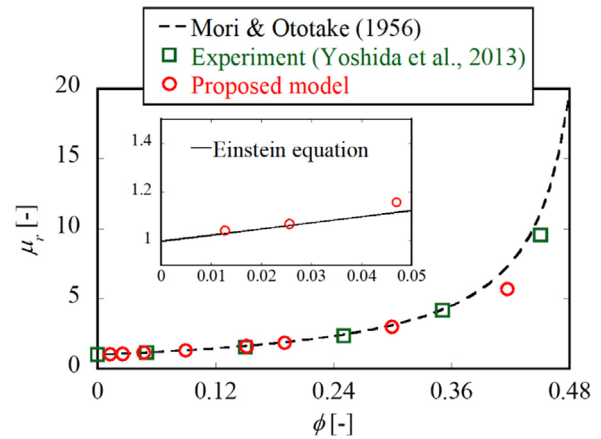


Fig. 17. Relative viscosity plotted with the packing fraction.

capture the complex hydrodynamic interactions between particles in suspensions up to relatively high packing fraction.

### 3.5. Simulation of fluidised bed

This section shows an application of the proposed model to the analyses of a liquid–solid fluidised bed. The schematic of the system is shown in Fig. 18. A superficial velocity  $U$  is applied at the bottom of the bed. The particles are randomly generated in the whole simulation domain with the initial packing fraction of 0.168. The periodic boundary conditions are applied in the  $x$ - and  $y$ -directions. The resolution to the effective radius is 15 so that the simulations are mesh-independent as shown in Fig. 10. The thickness parameter is  $d_p/60$  which is based on Fig. 11 with the packing fraction up to roughly 0.3.

Since the mixtures of particles with different density are commonly found in the application of fluidised bed [81], two cases are examined: uniform density (2500 kg/m<sup>3</sup>) and binary mixture (2000 and 3000 kg/m<sup>3</sup>) beds. Note that two beds have the same particle size. The volume ratio of the light to heavy particles for the binary mixture is 1 and they are uniformly mixed in the initial state. The average bed weight is the same between these two cases. The calculation conditions are shown in Table 2.

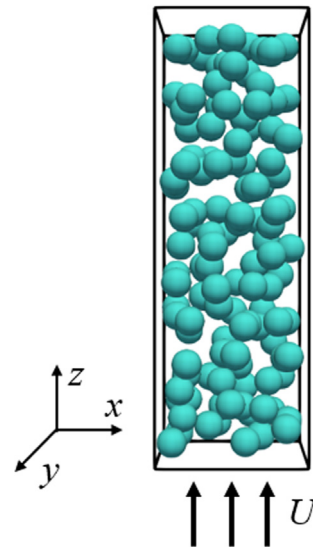


Fig. 18. Schematic of fluidised bed.

**Table 1**  
Calculation conditions for the prediction of relative viscosity of suspension.

Property	Value
Simulation domain [mm <sup>3</sup> ]	$7 \times 5 \times 7$
Thickness parameter [mm]	$d_p/80$
Particle diameter [mm]	1
Particle density [kg/m <sup>3</sup> ]	2500
Young's modulus [MPa]	5
Poisson's ration [-]	0.25
Restitution coefficient [-]	0.9
Friction coefficient [-]	0.3
Fluid dynamic viscosity [Pa · s]	0.01
Fluid density [kg/m <sup>3</sup> ]	1000

**Table 2**  
Calculation conditions for fluidised bed.

Property	Value
Simulation domain [mm <sup>3</sup> ]	30 × 30 × 90
Cell size [mm]	0.2
Thickness parameter [mm]	$d_p/60$
Particle diameter [mm]	6
Total number of particles [–]	120
Superficial velocity [m/s]	0.1
Young's modulus [MPa]	5
Poisson's ration [–]	0.25
Restitution coefficient [–]	0.9
Friction coefficient [–]	0.3
Fluid dynamic viscosity [Pa · s]	0.015
Fluid density [kg/m <sup>3</sup> ]	1000

When fluid flows through the particle bed, the pressure drop is commonly determined by the Ergun equation [82] in the following form:

$$\frac{\Delta p}{L} = \frac{\phi}{d_p(1-\phi)^3} \left[ 1.75\rho_f U^2 + \frac{150\phi\mu U}{d_p} \right] \quad (33)$$

where  $\Delta p$  is the pressure drop,  $L$  is length of the particle bed and  $U$  is the superficial velocity. When this is equivalent to the particles weight and buoyancy, Eq. (33) can be rewritten as:

$$\frac{\phi}{d_p(1-\phi)^3} \left[ 1.75\rho_f U^2 + \frac{150\phi\mu U}{d_p} \right] = \phi(\rho_p - \rho_f)g \quad (34)$$

Eq. (34) is solved with respect to  $\phi$  to estimate the packing fraction for the given conditions.

Snapshots of the uniform density and binary mixture beds from  $t = 0.02$ s to  $t = 3.0$ s are shown in Fig. 19. At the beginning, in both cases, the particles fall downwards due to the larger gravitational force as compared to the sum of the particle–fluid interaction and buoyancy forces since the packing fraction is low within the beds. In the binary mixture bed, the denser particles tend to fall faster and accumulate at the bottom of the bed. After the fluidisation regime is reached, i.e. the regime when the average bed height and the resultant concentration remain almost constant over time, the particles with different densities are completely segregated. The bulk height of the two cases is about the same in the fluidisation regime. The estimated packing fraction by Eq. (34) is  $\phi = 0.30$  and the average  $\phi$  over two seconds in the fluidisation regime in the simulation is 0.315 and 0.291 for the uniform density and binary mixture beds, respectively. It can be seen that the denser particles at lower layer of the binary mixture bed require the higher  $\phi$  so that the drag force is balanced with the particles weight, while the lighter particles at the upper layer give smaller  $\phi$ . However, as indicated by Eq. (34), the relationship between the drag force and

the packing fraction is non-linear. The non-linearity of the drag force may lead to the difference between  $\phi$  obtained by the uniform density and binary mixture beds. It is worth noting that the proposed model gives about 5% difference as compared to the Ergun equation.

#### 4. Conclusions

The resolved CFD–DEM coupling model with the VP method is proposed in this paper for the study of particulate flow. A smooth mask function is used to avoid numerical oscillation and optimal permeability is employed to improve the accuracy. To validate the proposed model, three kinds of simulations are performed: (i) the flow past a single particle, (ii) the flow through a periodic array and (iii) a particle approaching to a plane wall. The key findings in each validation are as follows:

- (i) In general, the proposed model can capture the particle–fluid interaction reasonably in the Reynolds number range tested (up to  $Re = 100$ ). The drag coefficients obtained are comparable to those reported in literature. The thickness parameter is not very sensitive to the computed drag coefficient especially for low Reynolds number flows. In this sense, employing a large thickness parameter is more advantageous since the stable time step limit is determined by the permeability. However, when the highest Reynolds number is used, the error becomes relatively large with the large thickness parameters (i.e.  $\delta = d_p/20$  and  $d_p/40$ ). This is because the boundary layer becomes thinner as the Reynolds number increases. This implies that an appropriately small thickness parameter should be chosen to apply the proposed model to high Reynolds number flows.
- (ii) It is proven that the effective pore radius  $r_{eff}$  is a good measure to check the mesh independency: simulation cell size needs to be at least 10 times smaller than  $r_{eff}$ . A smaller thickness parameter should be used as particle packing fraction increases since the fluid flow in the small gap between particles need to be resolved accurately. An appropriate thickness parameter for packing fraction up to 0.68 can be readily determined from Fig. 11 and Fig. 12.
- (iii) The simulation results indicate that the dominant factor is the thickness parameter: a smaller thickness parameter is required to capture the lubrication effect. It is also proven that the error of the fluid force to the exact solution can be universally characterised by the ratio between the gap and the thickness parameter: the error becomes about 5% when the ratio is 10 and becomes 10% roughly when the ratio is 5. These results can be used as a guideline for the further development of a lubrication force model.

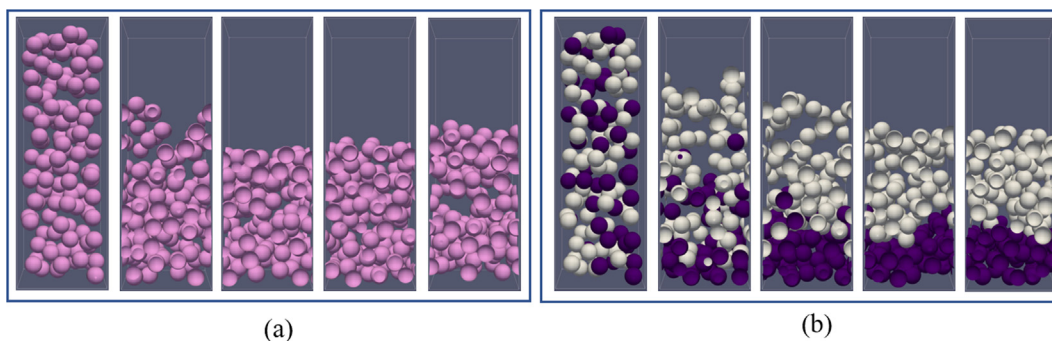


**Fig. 19.** Fluidisation of particles at 0.02, 0.4, 0.6, 1.0 and 3.0 second from the left to the right; (a) uniform density and (b) binary mixture beds. The particles coloured in white, pink and purple show 2000, 2500 and 3000 kg/m<sup>3</sup> particles, respectively. (For interpretation of the references to colour in this figure legend, the reader is referred to the web version of this article.)

Two applications of the proposed model are presented: the prediction of the relative viscosity of suspensions and the fluidised beds with uniform density and binary mixture particles. It is found that the proposed model is able to estimate the relative viscosity of the suspensions with the packing fraction up to 0.3. At higher packing fraction, however, noticeable difference from the experiment as well as the empirical model can be seen. The potential reasons are the lubrication effect as well as the effect of the top and bottom walls. The packing fractions of both the uniform density and binary mixture fluidised beds are  $\phi = 0.315$  and  $0.291$ , respectively, which are comparable to that estimated from the Ergun equation, i.e.  $\phi = 0.30$ . The difference between the particle volume fractions of the uniform density and binary mixture beds could be caused by the non-linear relationship between the drag force and the packing fraction. The results in this paper indicate that the resolved CFD-DEM model proposed is capable of simulating particulate flow from dilute to relatively dense system.

### Declaration of Competing Interest

The authors declare that they have no known competing financial interests or personal relationships that could have appeared to influence the work reported in this paper.

### Acknowledgment

The authors gratefully acknowledge the financial support from Japan International Cooperation Agency (JICA) through ASEAN University Network/Southeast Asia Engineering Education Development Network (AUN/SEED-Net) project. The authors would like to thanks Eric Hester in the University of Sydney for the fruitful discussions.

### References

- [1] D. Gidaspow, *Multiphase Flow and Fluidization: Continuum and Kinetic Theory Descriptions*, 1st ed., Academic Press, 1994.
- [2] J.A.M. Kuipers, K.J. van Duin, F.P.H. van Beckum, W.P.M. van Swaaij, Computer simulation of the hydrodynamics of a two-dimensional gas-fluidized bed, *Comput. Chem. Eng.* 17 (1993) 839–858.
- [3] T.B. Anderson, R. Jackson, A fluid mechanical description of fluidized beds: Comparison of Theory and Experiment, *Ind. Eng. Chem. Fundam.* 8 (1969) 137–144.
- [4] P.A. Cundall, O.D.L. Strack, A discrete numerical model for granular assemblies, *Geotechnique* 29 (1979) 47–65.
- [5] Y. Tsuji, T. Kawaguchi, T. Tanaka, Discrete particle simulation of two-dimensional fluidized bed, *Powder Technol.* 77 (1993) 79–87.
- [6] R. Beetstra, M.A. van der Hoef, J.A.M. Kuipers, Numerical study of segregation using a new drag force correlation for polydisperse systems derived from lattice-Boltzmann simulations, *Chem. Eng. Sci.* 62 (2007) 246–255.
- [7] K. Washino, H.S. Tan, M.J. Hounslow, A.D. Salman, Meso-scale coupling model of DEM and CIP for nucleation processes in wet granulation, *Chem. Eng. Sci.* 86 (2013) 25–37.
- [8] R. Sun, H. Xiao, Diffusion-based coarse graining in hybrid continuum-discrete solvers: Theoretical formulation and a priori tests, *Int. J. Multiph. Flow* 77 (2015) 142–157.
- [9] Y. Mino, S. Sakai, H. Matsuyama, Simulations of particulate flow passing through membrane pore under dead-end and constant-pressure filtration condition, *Chem. Eng. Sci.* (2018).
- [10] K. Murase, T. Mochida, Y. Sagawa, H. Sugama, Estimation on the strength of a liquid bridge adhered to three spheres, *Adv. Powder Technol.* 19 (2008) 349–367.
- [11] N.G. Deen, M. van, S. Annaland, J.A.M. Kuipers, Direct numerical simulation of complex multi-fluid flows using a combined front tracking and immersed boundary method, *Chem. Eng. Sci.* 64 (2009) 2186–2201.
- [12] K. Washino, H.S. Tan, A.D. Salman, M.J. Hounslow, Direct numerical simulation of solid-liquid-gas three-phase flow: Fluid-solid interaction, *Powder Technol.* 206 (2011) 161–169.
- [13] K. Washino, H.S. Tan, M.J. Hounslow, A.D. Salman, A new capillary force model implemented in micro-scale CFD-DEM coupling for wet granulation, *Chem. Eng. Sci.* 93 (2013) 197–205.
- [14] M. Fujita, O. Koike, Y. Yamaguchi, Direct simulation of drying colloidal suspension on substrate using immersed free surface model, *J. Comput. Phys.* 281 (2015) 421–448.
- [15] H. Kan, H. Nakamura, S. Watano, Numerical simulation of particle-particle adhesion by dynamic liquid bridge, *Chem. Eng. Sci.* 138 (2015) 607–615.
- [16] X. Sun, M. Sakai, Direct numerical simulation of gas-solid-liquid flows with capillary effects: An application to liquid bridge forces between spherical particles, *Phys. Rev. E* 94 (2016) 1–22.
- [17] H. Kan, H. Nakamura, S. Watano, Effect of collision angle on particle-particle adhesion of colliding particles through liquid droplet, *Adv. Powder Technol.* 29 (2018) 1317–1322.
- [18] Y. Mino, H. Shinto, Lattice Boltzmann method for simulation of wettable particles at a fluid-fluid interface under gravity, *Phys. Rev. E* (2020).
- [19] J. Gu, S. Takeuchi, T. Kajishima, Influence of Rayleigh number and solid volume fraction in particle-dispersed natural convection, *Int. J. Heat Mass Transf.* 120 (2018) 250–258.
- [20] K. Kushimoto, S. Ishihara, J. Kano, Development of ADEM-CFD model for analyzing dynamic and breakage behavior of aggregates in wet ball milling, *Adv. Powder Technol.* 30 (2019) 1131–1140.
- [21] A. Loseille, Unstructured Mesh Generation and Adaptation, in: R. Abgrall, C.-W. Shu (Eds.), *Handb. Elsevier, Numer. Methods Hyperbolic Probl.*, 2017, pp. 263–302.
- [22] J. Tu, G.-H. Yeoh, C. Liu, J. Tu, G.-H. Yeoh, C. Liu, CFD Mesh Generation: A Practical Guideline, in: *Comput. Fluid Dyn.*, Butterworth-Heinemann (2018) 125–154.
- [23] C.S. Peskin, Numerical analysis of blood flow in the heart, *J. Comput. Phys.* 25 (1977) 220–252.
- [24] E.R. Mittal, G. Iaccarino, Immersed boundary methods, *Annu. Rev. Fluid Mech.* 37 (2005) 239–261.
- [25] R.P. Beyer, R.J. Leveque, Analysis of a one-dimensional model for the immersed boundary method, *SIAM J. Numer. Anal.* 29 (1992) 332–364.
- [26] J. Mohd-Yusof, Combined immersed boundary/B-spline methods for simulation of flow in complex geometries, *Cent. Turbul. Res. Annu. Res. Briefs* 1 (1997) 171–186.
- [27] J. Kim, D. Kim, H. Choi, An Immersed-Boundary Finite-Volume Method for Simulations of Flow in Complex Geometries, *J. Comput. Phys.* 171 (2001) 132–150.
- [28] Y.H. Tseng, J.H. Ferziger, A ghost-cell immersed boundary method for flow in complex geometry, *J. Comput. Phys.* 192 (2003) 593–623.
- [29] J.K. Patel, G. Natarajan, Diffuse interface immersed boundary method for multi-fluid flows with arbitrarily moving rigid bodies, *J. Comput. Phys.* 360 (2018) 202–228.
- [30] D. Kim, H. Choi, Immersed boundary method for flow around an arbitrarily moving body, *J. Comput. Phys.* 212 (2006) 662–680.
- [31] F. Domenichini, On the consistency of the direct forcing method in the fractional step solution of the Navier-Stokes equations, *J. Comput. Phys.* (2008).
- [32] N. Sato, S. Takeuchi, T. Kajishima, M. Inagaki, N. Horinouchi, A consistent direct discretization scheme on Cartesian grids for convective and conjugate heat transfer, *J. Comput. Phys.* 227 (2016) 6372–6384.
- [33] D. Goldstein, R. Handler, L. Sirovich, Modeling a No-Slip Flow Boundary with an External Force Field, *J. Comput. Phys.* 105 (1993) 354–366.
- [34] M.C. Lai, C.S. Peskin, An immersed boundary method with formal second-order accuracy and reduced numerical viscosity, *J. Comput. Phys.* 160 (2000) 705–719.
- [35] E.M. Saiki, S. Biringen, Numerical simulation of a cylinder in uniform flow: Application of a virtual boundary method, *J. Comput. Phys.* 123 (1996) 450–465.
- [36] P. Angot, C.H. Bruneau, P. Fabrie, A penalization method to take into account obstacles in incompressible viscous flows, *Numer. Math.* 81 (1999) 497–520.
- [37] G. Carbou, P. Fabrie, Boundary layer for a penalization method for viscous incompressible flow, *Adv. Differ. Equations* 8 (2003) 1453–1480.
- [38] K. Schneider, Numerical simulation of the transient flow behaviour in chemical reactors using a penalisation method, *Comput. Fluids* 34 (2005) 1223–1238.
- [39] K. Guo, X. Cui, M. Liu, A Coupled Lattice Boltzmann-Volume Penalization for Flows Past Fixed Solid Obstacles with Local Mesh Refinement, *Math. Probl. Eng.* 2018 (2018) 1–12.
- [40] D. Kolomenskiy, K. Schneider, A Fourier spectral method for the Navier-Stokes equations with volume penalization for moving solid obstacles, *J. Comput. Phys.* 228 (2009) 5687–5709.
- [41] K. Schneider, Immersed boundary methods for numerical simulation of confined fluid and plasma turbulence in complex geometries: A review, *J. Plasma Phys.* 81 (2015) 1–21.
- [42] M. Specklin, Y. Delauré, A sharp immersed boundary method based on penalization and its application to moving boundaries and turbulent rotating flows, *Eur. J. Mech. B/Fluids* 70 (2018) 130–147.
- [43] B. Lambert, L. Weynans, M. Bergmann, Local lubrication model for spherical particles within incompressible Navier-Stokes flows, *Phys. Rev. E* 97 (2018) 1–16.
- [44] B. Lambert, L. Weynans, M. Bergmann, Methodology for numerical simulations of ellipsoidal particle-laden flows, *Int. J. Numer. Methods Fluids* 92 (2020) 855–873.
- [45] B. Kadoch, D. Kolomenskiy, P. Angot, K. Schneider, A volume penalization method for incompressible flows and scalar advection-diffusion with moving obstacles, *J. Comput. Phys.* 231 (2012) 4365–4383.
- [46] C. Jause-Labert, F.S. Godeferd, B. Favier, Numerical validation of the volume penalization method in three-dimensional pseudo-spectral simulations, *Comput. Fluids* 67 (2012) 41–56.

- [47] T. Engels, D. Kolomenskiy, K. Schneider, J. Sesterhenn, Two-dimensional simulation of the fluttering instability using a pseudospectral method with volume penalization, *Comput. Struct.* 122 (2013) 101–112.
- [48] W. Iwakami, Y. Yatagai, N. Hatakeyama, Y. Hattori, A new approach for error reduction in the volume penalization method, *Commun. Comput. Phys.* 16 (2014) 1181–1200.
- [49] D. Kolomenskiy, R. Nguyen Van Yen, K. Schneider, Analysis and discretization of the volume penalized Laplace operator with Neumann boundary conditions, *Appl. Numer. Math.* 95 (2015) 238–249.
- [50] T. Engels, D. Kolomenskiy, K. Schneider, J. Sesterhenn, Numerical simulation of fluid–structure interaction with the volume penalization method, *J. Comput. Phys.* 281 (2015) 96–115.
- [51] C. Bernier, M. Gazzola, R. Ronsse, P. Chatelain, Simulations of propelling and energy harvesting articulated bodies via vortex particle-mesh methods, *J. Comput. Phys.* 392 (2019) 34–55.
- [52] K.J. Burns, D. Lecoanet, G.M. Vasil, J.S. Oishi, B.P. Brown, The “Sphered Cube”: A New Method for the Solution of Partial Differential Equations in Cubical Geometry, (2019). [arxiv.org/abs/1903.12642](https://arxiv.org/abs/1903.12642) (accessed March 29, 2019).
- [53] E.W. Hester, G.M. Vasil, K.J. Burns, Improving convergence of volume penalized fluid-solid interactions, (2020). [arxiv.org/abs/1903.11914](https://arxiv.org/abs/1903.11914) (accessed June 10, 2020).
- [54] Y. Tsuji, T. Tanaka, T. Ishida, Lagrangian numerical simulation of plug flow of cohesionless particles in a horizontal pipe, *Powder Technol.* 71 (1992) 239–250.
- [55] G.F.F. G. Hertz’s miscellaneous papers, *Nature*. 55 (1896) 6–9.
- [56] R.D. Mindlin, Compliance of elastic bodies in contact, *J. Appl. Mech.* 16 (1949) 259–268.
- [57] A. Passalacqua, R.O. Fox, Implementation of an iterative solution procedure for multi-fluid gas-particle flow models on unstructured grids, *Powder Technol.* 213 (2011) 174–187.
- [58] R.I. Issa, B. Ahmadi-Befrui, K.R. Beshay, A.D. Gosman, Solution of the implicitly discretised reacting flow equations by operator-splitting, *J. Comput. Phys.* 93 (1991) 388–410.
- [59] S.V. Patankar, *Numerical heat transfer and fluid flow*, Taylor & Francis, 1980.
- [60] Y. Li, Y. Xu, C. Thornton, A comparison of discrete element simulations and experiments for “sandpiles” composed of spherical particles, *Powder Technol.* (2005).
- [61] L. Schiller, Z. Naumann, A drag coefficient correlation, *Z. Ver. Deutsch. Ing.* 77 (1935) 318–320.
- [62] C. Jause Labert, Simulation numérique d’écoulements turbulents en rotation, confinement et forçage à l’aide d’une méthode de pénalisation, L’Université de Lyon (2012).
- [63] A.A. Zick, G.M. Homsy, Stokes flow through periodic arrays of spheres, *J. Fluid Mech.* 115 (1982) 13–26.
- [64] S. Middleman, *Capillary Penetration Dynamics*, in: *Model. Axisymmetric Flows Dyn. Film. Jets, Drops*, Academic Press, San Diego, 1995: pp. 211–239.
- [65] M. Denesuk, G.L. Smith, B.J.J. Zelinski, N.J. Kreidl, D.R. Uhlmann, Capillary penetration of liquid droplets into porous materials, *J. Colloid Interface Sci.* 158 (1993) 114–120.
- [66] J. Kozeny, Über kapillare Leitung des Wassers im Boden, *Sitzungsber. Akad. Wiss. Wien.* 136 (2a) (1927) 271–306.
- [67] H. Brenner, The slow motion of a sphere through a viscous fluid towards a plane surface, *Chem. Eng. Sci.* 16 (1961) 242–251.
- [68] S.L. Dance, M.R. Maxey, Incorporation of lubrication effects into the force-coupling method for particulate two-phase flow, *J. Comput. Phys.* 189 (2003) 212–238.
- [69] J.A. Simeonov, J. Calantoni, Modeling mechanical contact and lubrication in Direct Numerical Simulations of colliding particles, *Int. J. Multiph. Flow.* 46 (2012) 38–53.
- [70] K. Washino, S. Hashino, H. Midou, E.L. Chan, T. Tsuji, T. Tanaka, Lubrication force model for a pendular liquid bridge of power-law fluid between two particles, *Chem. Eng. Res. Des.* 132 (2018) 1030–1036.
- [71] E. Biegert, B. Vowinkel, E. Meiburg, A collision model for grain-resolving simulations of flows over dense, mobile, polydisperse granular sediment beds, *J. Comput. Phys.* 340 (2017) 105–127.
- [72] J. Gu, M. Sakaue, S. Takeuchi, T. Kajishima, An immersed lubrication model for the fluid flow in a narrow gap region, *Powder Technol.* 329 (2018) 445–454.
- [73] J.J. Stickel, R.L. Powell, Fluid mechanics and rheology of dense suspensions, *Annu. Rev. Fluid Mech.* 37 (2005) 129–149.
- [74] M. Maxey, Simulation Methods for Particulate Flows and Concentrated Suspensions, *Annu. Rev. Fluid Mech.* 49 (2017) 171–193.
- [75] J. Topping, Investigations on the Theory of the Brownian Movement, *Phys. Bull.* (1956).
- [76] M. Kunitz, Empirical formula for the relation between viscosity of solution and volume of solute, *J. Gen. Physiol.* 9 (1926) 715–725.
- [77] M. Mooney, The viscosity of a concentrated suspension of spherical particles, *J. Colloid Sci.* 6 (1951) 162–170.
- [78] T.F. Ford, Viscosity-concentration and fluidity-concentration relationships for suspensions of spherical particles in Newtonian liquids, *J. Phys. Chem.* 64 (1960) 1168–1174.
- [79] Y. Yoshida, T. Katsumoto, S. Taniguchi, A. Shimosaka, Y. Shirakawa, J. Hidaka, Prediction of viscosity of slurry suspended fine particles using coupled DEM-DNS simulation, *Chem. Eng. Trans.* 32 (2013) 2089–2094.
- [80] Y. Mori, N. Ootake, On the Viscosity of Suspensions, *Chem. Eng.* 20 (1956) 488–494.
- [81] P.N. Rowe, A.W. Nienow, Particle mixing and segregation in gas fluidised beds, A review, *Powder Technol.* 15 (1976) 141–147.
- [82] S. Ergun, Fluid flow through packed columns, *Chem. Eng. Prog.* 48 (1952) 89–94.